In Situ Fracture Behavior of Single Crystal LiNi$_{0.8}$Mn$_{0.1}$Co$_{0.1}$O$_2$ (NMC811)

Laura Wheatcroft,[a, b] Arron Bird,[a] Naresh Gollapally,[a, b] Samuel G. Booth,[a, b] Serena A. Cussen,[a, b] and Beverley J. Inkson*[a, b]

Single crystal particle morphologies have become highly desirable for next generation cathode materials, removing grain boundary fracture and thereby reducing the surface area exposed to electrolyte. The intrinsic mechanical behavior of single crystal layered oxides, however, is poorly understood. Here, faceted single crystal LiNi$_{0.8}$Mn$_{0.1}$Co$_{0.1}$O$_2$ (NMC811) particles are compressed in situ in a scanning electron microscope (SEM), to determine mechanical deformation mechanisms as a function of crystallographic orientation. In situ, the dynamical deformation sequence observed is initial cracking at the compression zone, followed by accelerated transparticle crack propagation and concurrent (0001) slip band formation. The greatest loads and contact pressure at fracture, non-basal

cracking, and activation of multiple basal slip systems in larger (>3 μm) particles, occur for compression normal to the (0001) layered structure. Loading on {012} preferentially activates basal fracture and slip at lower loads. Regardless of particle orientation, non-basal slip systems are not observed, and non-basal cracking and particle rotation occur during compression to compensate for this inability to activate dislocations in 3-dimensions. Crystallographic dependent mechanical behaviour of single crystal NMC811 means that particle texture in cathodes should be monitored, and sources of localised surface stress in cathodes, e.g. particle-to-particle asperity contacts during electrode manufacture, should be minimised.

1. Introduction

LiNi$_{0.8}$Mn$_{0.1}$Co$_{0.1}$O$_2$ (NMC811) has gained attention as a Lithium ion battery (LiB) cathode material for high energy applications.[1] NMC811 has been successfully commercialised with improvements in doping, coating and morphology helping to extend lifetime and range, whilst reducing the overall cost by lowering the Co content.[1,2] However, NMC811 is susceptible to reduced lifetime, and voltage limitations which become exacerbated at higher Ni contents.[1,3] Reasons for reduced lifetimes are varied, including oxygen loss,[4] rock salt formation creating an insulating reduced surface layer,[4,5] fracture[6,7] linked to a c-axis collapse at high states of charge,[3,8,9] and surface layer formation.[7] Fracture has also been found to result from manufacture of electrodes, due to calendering, and mixing.[3,10]

The most common commercial NMC811 particle morphology is a polycrystalline secondary particle, a sphere of NMC811 (diameters ranging from 5–20 μm) consisting of primary grains

of NMC811. Polycrystalline NMC811 particles suffer from intergranular fracture during cycling, resulting in reduced cathode lifetime.[3,11] NMC811 primary grains, and other layered lattice materials, undergo anisotropic shape change, swelling and contraction upon delithiation.[6,9,12,13] In a polycrystalline morphology the primary particle shrinkage and shape change is constrained, resulting in stress states which leads to intergranular crack formation.[12,14] Upon cracking, fresh particle surface is exposed to corrosion from the electrolyte, resulting in chemo-mechanical degradation of the cathode.[14]

Single crystal NMC811 is seen as a potential morphology to avoid intergranular fracture due to a significant reduction in grain boundaries. However, single crystal NMC is still vulnerable to intragranular fracture during the electrode calendering process and during cycling when charged to high potentials.[3,15,16] Stallard *et al.* estimated that the basal shear strength of fully lithiated single crystal NMC811 is very low at 86 MPa,[15] which is less than that of polycrystalline NMC811 at 180 MPa,[17] leaving single crystal NMC811 particles vulnerable to slip under light loads. Micro-fractures have also been observed in single crystal NMC morphologies when charging to higher potentials,[18,19] as well as basal (0001) slip band formation.[5,19,20]

The layered transition metal oxide NMC811 has a highly anisotropic trigonal crystal structure ($R\bar{3}m$) as shown in Figure 1, with the c-axis significantly longer than the a-axis (14.26 Å and 2.87 Å respectively).[9] Previous nanoindentation measurements on a range of sintered NMC materials with different Ni, Mn, and Co contents confirmed that the low symmetry of the unit cell is associated with anisotropic elastic stiffness, with the Young's modulus being greatest along the [0001] direction.[16]

[a] L. Wheatcroft, A. Bird, N. Gollapally, S. G. Booth, S. A. Cussen, B. J. Inkson
Department of Materials Science and Engineering
University of Sheffield
Mappin Street, Sheffield, S1 3JD, United Kingdom
E-mail: beverley.inkson@sheffield.ac.uk

[b] L. Wheatcroft, N. Gollapally, S. G. Booth, S. A. Cussen, B. J. Inkson
The Faraday Institution
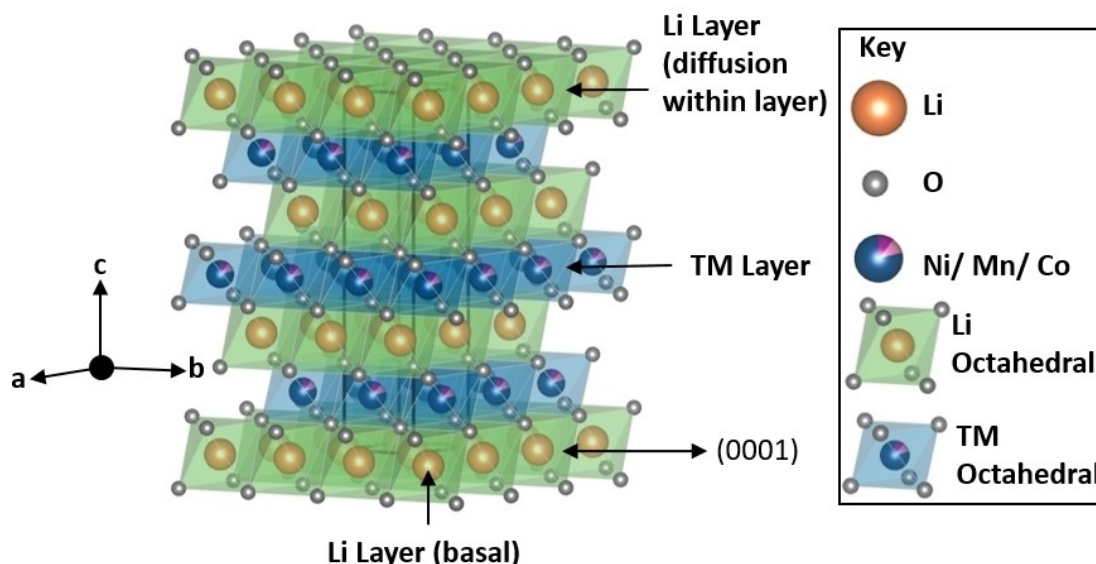Quad One, Harwell Campus, Didcot, OX11 0RA, United Kingdom

Figure 1. Schematic of the NMC811 lattice with the R$\bar{3}$m unit cell outlined. The orange spheres represent the Li atoms, with the (0001) basal plane highlighted. Cyan, magenta, and pink spheres represent Ni, Mn, and Co atoms respectively. Grey spheres represent oxygen atoms.

The slip systems for pristine NMC811 have to date not been specifically defined, but have been investigated for the analogous LiCoO$_2$ structure, an R$\bar{3}$m structure similar to NMC811 except with only Co in the transition metal layer. Gabrisch *et al.* concluded that LiCoO$_2$ has a singular easily activated basal (0001) slip plane, with a glissile Burgers vector $\mathbf{b} = \frac{a}{3} < 11\bar{2}0 > (0001)$.[21] When examining cycled high Ni content NMC materials, the slip mechanism is complicated by ion diffusion and surface rock salt formation.[5] Evidence of basal glide has been observed in high Ni content NMC materials in a charged state, with the observation of slip steps, or surface reconstruction to form $(\bar{1}08)$ facets associated with rock salt formation.[5]

To date there is little understanding of how the R$\bar{3}$m structure, and anisotropic elastic mechanical properties of NMC materials,[16] affect plastic deformation and fracture in single crystal NMC811 materials. Understanding particle-level fracture mechanisms is important as the chemical interactions at freshly exposed particle surfaces after fracture is a major contributor to reduced cathode lifetimes.[12,14]

Here, in situ compression testing is used for the first time to track the real-time sequence of particle deformation and cracking mechanisms in NMC811 single crystal particles as a function of their crystallographic orientation. Specifically, microindentation compression testing is performed on individual faceted single crystal NMC811 particles with known facet crystallography, using an in situ scanning electron microscopy (SEM) technique developed in,[11] and pristine faceted single crystal NMC811 particles developed in.[22] The load applied at particle fracture is measured for each NMC811 facet compression test, and the plastic deformation/fracture mechanisms are dynamically imaged by SEM during the test, enabling the dependence of slip and cracking activation/propagation on the crystallographic orientation of NMC materials with respect to loading direction to be understood for the first time. Particle

compression here is performed using a cono-spherical diamond tip, representing stresses induced by asperity particle-particle contacts during electrode processing (calendering, pressing or mixing), and/or surface stress formation via processes such surface phase formation during cycling. For both roll calendering and cold-pressing, as the degree of slurry compaction goes up (higher applied average pressures), more active particles will come into contact, and the probability that very high local pressures occur at sharp asperity contacts leading to particle deformation will increase. A detailed understanding of cathode particle mechanical properties is key for the optimisation of electrode manufacture and operation, to increase the performance and longevity of industrially relevant next generation cathode materials.

2. Results and Discussion

2.1. In Situ SEM Microindentation of Single Crystal NMC811

SEM imaging of the synthesised single crystal NMC811 confirmed a primarily faceted particle morphology with a predominantly truncated octahedral shape (Figure 2(a)). Only faceted particles were selected for compression using the in situ SEM mounted microindenter rig, by secondary electron (SE) imaging performed prior to compression. The size range of particles compression tested in this study was from 2.5–3.9 μm (maximum dimension, measured lengthways apex-to-apex).

TEM imaging and SAED was used to identify the facet planes of the octahedral NMC811 particles. A representative particle, with SAED pattern down the $[2\bar{2}01]$ zone axis and the corresponding TEM image, is shown in Figure 2(b). The large faces on the truncated octahedrons consist of facets from the (0001) and $\{01\bar{1}2\}$ ($\{012\}$) families. The corners of the truncated octahedrons are rounded and close to $\{10\bar{1}4\}$ ($\{104\}$) planes. A
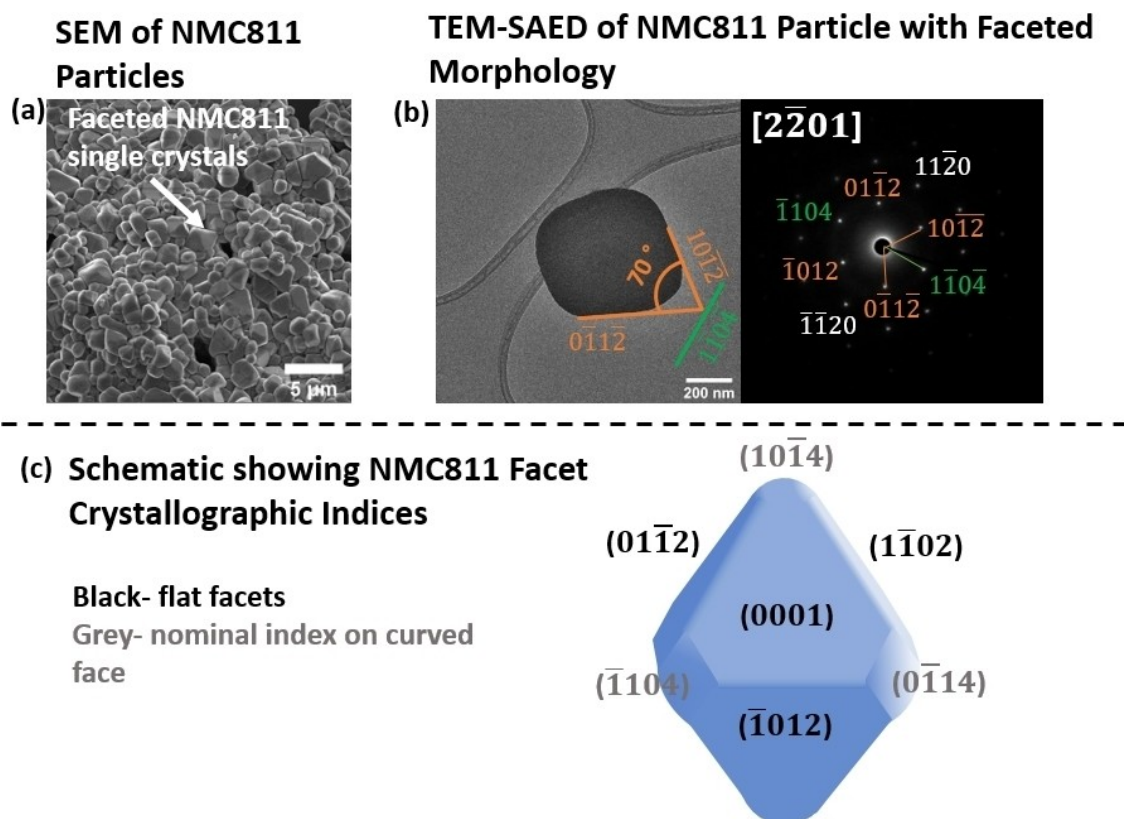
Figure 2. (a) SEM images of the faceted single crystal NMC811 particles, (b) TEM image of a single crystal faceted NMC811 particle, and the corresponding SAED pattern down the $[2\bar{2}01]$ zone axis. (c) Schematic showing the NMC811 facet indices as identified through TEM-SAED.

schematic showing the facet indices is shown in Figure 2(c). The (0001), {012} and {104} facet planes of the truncated octahedral NMC811 particles analysed in this study (Figure 2) are consistent with those previously reported.[23]

To understand how crystal orientation and morphology affects the deformation and fracture behavior of NMC811, similarly sized particles were indented on different crystallographic facets using in situ SEM (Figure 3). Animated GIF's showing the in situ particle compression videos are available in the supporting information (GIF 1–3). Due to their octahedral shape, the NMC811 particles lay with either the (0001) or {012} facets on, or parallel to, the underlying Si substrate (Figure 2(c)). The easy slip plane for the $R\bar{3}m$ structure and NMC811 has been previously identified as the basal (0001) plane,[15,19,21] and is highlighted in the crystal structure schematics in Figure 3(c) and (f). For the in situ microindentation tests, the crystallography of the indented facets was identified from the SEM images based on the angle of the (0001) slip plane to the applied load axis/ indented facet (Figure 3(b) and (e)). Thus an applied load perpendicular to {012} would initially result in (0001) slip planes at 70° to the facet, whilst the (0001) slip planes would be parallel to the (0001) facet and the underlying Si wafer (see Figure 3(c) and (f)).

For the NMC811 truncated octahedral particles under investigation, the {104} family facets were small, and not clearly defined, positioned at the corners of the single crystal particles. Therefore, it was not possible to indent onto these {104} facets

due to the way particles settled onto the Si wafer when drop cast.

Figure 3 shows typical SEM images of NMC811 particles indented on (0001) and {012} facets before and after fracture (see also animated GIF 1–3, supporting information). Post-compression, distinct (0001) slip steps are visible on the surface of both particles in Figure 3(b) and Figure 3(e). These slip steps are consistent with the activation of the glissile $\mathbf{b} = \frac{a}{3} < 11\bar{2}0 > (0001)$ slip systems; a schematic showing the three basal slip systems is shown in Figure 4(g), with (0001) having been identified in previous studies[21] as the preferred slip plane. For the particle in Figure 3(b) the slip planes are parallel to the indented facet/ Si substrate, thus the facet indented in Figure 3(a) is (0001) (shown in Figure 3(c)). Note that Figure 3(a) demonstrates that the indented facet was not completely flat, with a small degree of curvature at the nanoscale.

For the NMC811 particle in Figure 3(d,e), the activated (0001) slip planes are at a steep angle, θ, to the indented facet, indicating that indentation was performed on a {012} facet (shown in Figure 3(f)). Post-indentation, it was not possible to accurately measure the angle of the slip planes in Figure 3(e) as the SEM image is a 2D projection of a 3D particle, and there was some rotation of particle fragments during deformation.

The dynamical SEM imaging of the NMC811 particle compression tests was used to evaluate the sequence of nanoscale deformation and fracture mechanisms. In situ videos
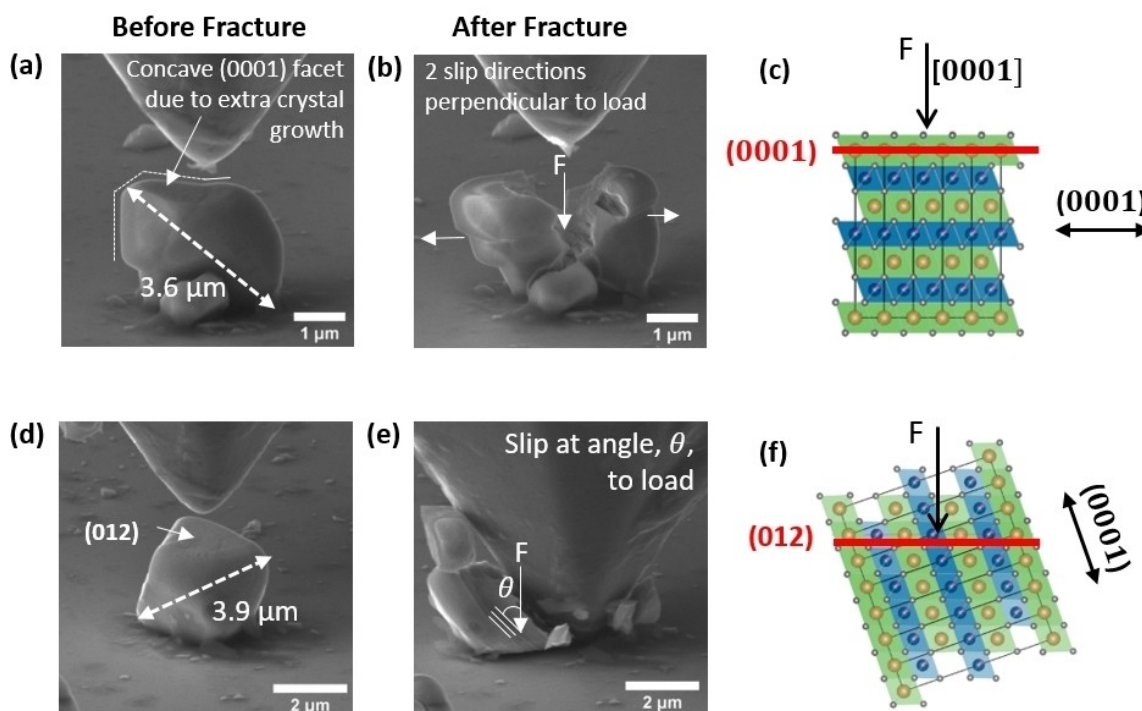
Figure 3. SEM images of NMC811 particles indented on (0001) and {012} facets before fracture (a) and (d) respectively, and after fracture (b) and (e). (c,f) Schematics showing the loading direction F on the crystal structure are shown in (c) for (0001) and (f) for {012} respectively. The (0001) slip plane orientations are indicated by the black arrows in (c) and (f). Basal slip occurs perpendicular to load direction, F, for indentation of the (0001) facet, and at an angle, θ, for indentation of the {012} facet.

of the full compression tests are available in the supporting information as animated GIFs (GIF 1–3). SEM images taken during compression of the (0001) facet are shown in Figure 4(a–d), with the corresponding load-displacement curve in Figure 4(e). Initially the load on the (0001) facet increases linearly with displacement until a small load drop occurs at 3.2 mN, when a crack initiates from the indenter tip-particle contact zone (Figure 4(b, e)) to reduce stress. This initial crack is nearly perpendicular to (0001), running approximately parallel to the [0001] load axis. Thereafter, the load increases again from 3.2 mN to 4.6 mN, with the vertical crack continuing to open and extend from the indentation point down 700 nm into the particle (Figure 4(c)). At 4.6 mN the stress is sufficient to first initiate two major (0001) slip bands either side of the crack that cleaves the top 700 nm of the NMC811 particle in two, and each piece slips sideways on (0001) in opposing directions. This then enables the indenter tip to quickly penetrate the particle like a wedge (Figure 4(d)), and the non-basal crack propagates fast down through the whole particle together with further activation of multiple (0001) slip bands (Figure 4(d)). Similar behavior was seen in other particles indented into the (0001) facet.

Figure 4(h–k) shows SEM images taken during compression of a NMC811 particle on a {012} facet, with the corresponding load-displacement curve in Figure 4(f). Initially the load on {012} increases linearly with displacement, but at a higher gradient (higher stiffness) than compression into the (0001) facet (comparing Figure 4(e) and (f)). Similar to the (0001) facet, a small load drop occurs at 2.5 mN Figure 4(f), which is due to

initiation of a small stress-relieving crack adjacent to the indenter contact zone (Figure 4(i, j)). The load resumes increasing, this time non-linearly with displacement, indicative of plasticity occurring to reduce stress, including the slow propagation of the visible crack. At 3.5 mN, rapid crack propagation down through a (0001) plane suddenly occurs, which completely cleaves a fragment of the particle. This causes a significant load drop from 3.5 mN to 1.6 mN, and the indenter compresses the remaining particle fragment (Figure 4(k)). After the partial particle fracture, the indenter remains in contact with the remainder of the {012} facet and continues compressing the particle. Small < 0.3 mN load drops in the remaining loading sequence are consistent with the activation of multiple (0001) slip bands, visible to the left of the indenter contact zone (Figure 4(k)), which enables the crystal to displace left and downwards (like a sliding pack of cards) to accommodate the vertical indenter displacement and reduce local stress.

Comparing the (0001) and {012} load curves (Figure 4(e,f)), the particle compressed on the (0001) facet underwent initial cracking at 3.2 mN, and then major fracture/ basal slip at 4.6 mN, which are higher loads than for a similar sized particle compressed on the {012} facet (2.5 mN and 3.5 mN respectively). Assuming the diamond indenter is axisymmetric, the mean contact pressure p_m at peak loads P_f can be estimated using the indenter-NMC particle contact radius directly measured from the in situ SEM imaging. For compression down [0001] the mean contact pressure at maximum load (Fig 4(c,e)) is $p_m = 14$ GPa, and for compression on the {012} facet $p_m =$
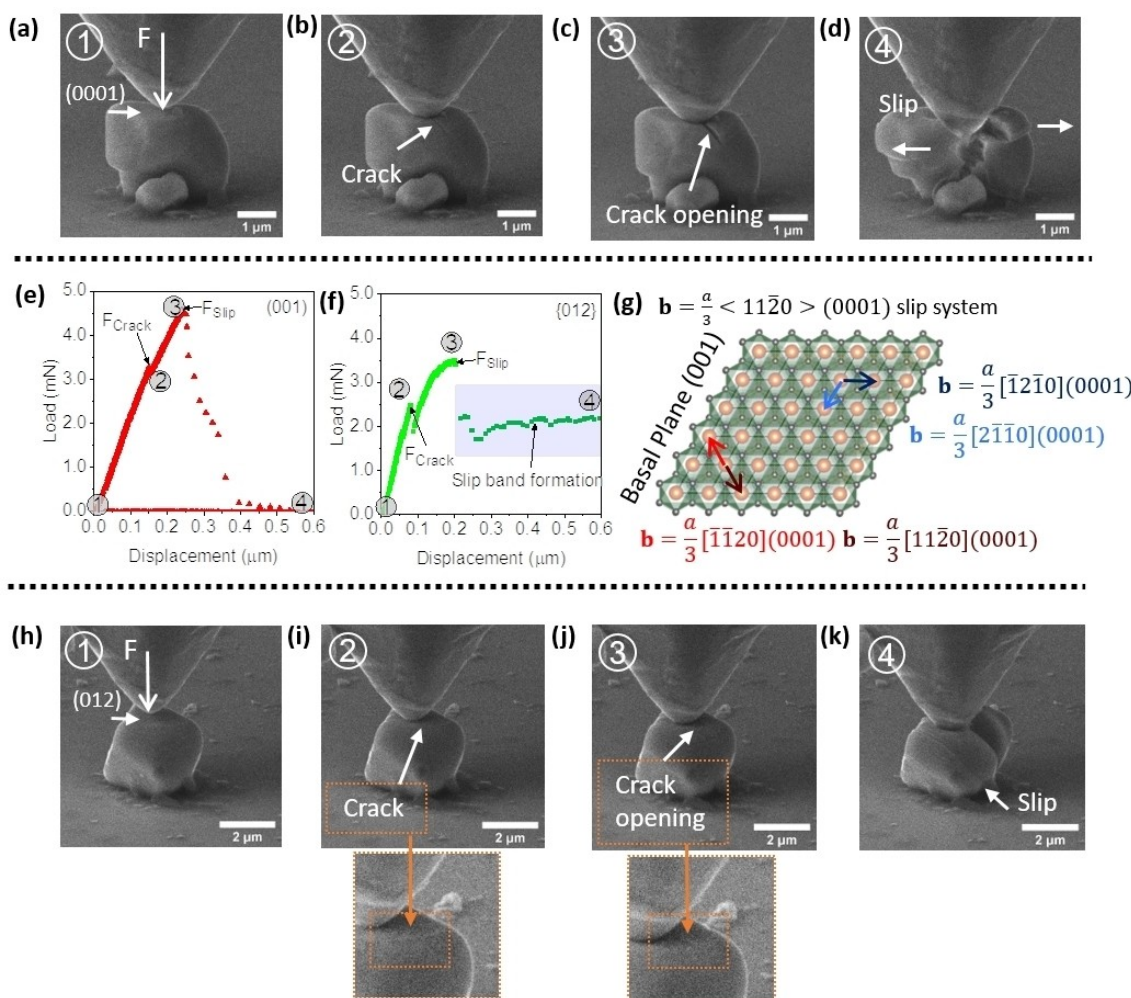
Batteries & Supercaps

Research Article
doi.org/10.1002/batt.202400077

**Chemistry
Europe**
European Chemical
Societies Publishing

Figure 4. (a–d) SEM images taken during indentation perpendicular to a NMC811 (0001) facet, from points 1, 2, 3, and 4 indicated on the corresponding load displacement curve in (e). (a) Point 1, start of load, (b) Point 2, initiation of non-basal surface crack, (c) Point 3, opening of surface crack, (d) Point 4, transparticle non-basal fracture and basal slip bands (two directions). (e,f) Load-displacement curves for the particles compressed on the (0001) facet (e), and {012} facet (f). (g) Schematic of the basal plane (0001) indicating the $\mathbf{b} = \frac{a}{3} < 11\bar{2}0 >$ Burgers vectors observed in (d) and (k). (h–k) SEM images taken during indentation perpendicular to the NMC811 {012} facet, from points 1, 2, 3, and 4 indicated on the corresponding load displacement curve in (f). (h) Point 1, start of load, (i) Point 2, initiation of surface crack, (j) Point 3, opening of surface crack, (k) Point 4, (0001) basal crack propagation and parallel slip band formation through whole particle.

11 GPa, which are comparable to the reported hardness H = 14 ± 3 GPa of sintered NMC811.[16]

A higher load to activate slip for loading on the (0001) plane is consistent with Schmid's law where the closer to perpendicular the load direction is to the shear direction, the higher the load required to activate slip. The fact that any basal glide is able to occur on the sample compressed almost normal to the (0001) facet, parallel to the glide plane (0001), is consistent with a relatively low basal shear stress of NMC811 single crystals estimated to be $\tau = 86$ MPa.[15]

The activation of (0001) slip by [0001] loading is also a consequence of the lack of alternative slip systems. In the $R\bar{3}m$ structure of NMC811 and related layered LiTMO$_2$ oxides the $b = \frac{a}{3} < 11\bar{2}0 > (0001)$ slip systems (Figure 4(g)) have $\mathbf{b} = \frac{a}{3} < 11\bar{2}0 >$ which is the only glissile, low displacement perfect Burgers vector.[21] Alternative slip systems involving significantly larger non-basal dislocations e.g. $\mathbf{b} = [0001]$, or

$\mathbf{b} = \frac{1}{3} < 11\bar{2}3 >$,[21] have not been detected here in the mechanical testing of pristine single crystal NMC811 particles. In particular, there is no evidence of slip steps growing on the basal facets of the NMC811 (see Figure 4(d) and (k)), signifying that only dislocations with Burgers vectors lying in (0001) are activated ($\mathbf{b} = \frac{a}{3} < 11\bar{2}0 > (0001)$). This inability to shear in three dimensions will be a driving force for stress relief by non-basal cracking and particle rotation (Figure 4(b–d, k)).

During compression of NMC811 particles on both the (0001) facet, and the {012} facets multiple (0001) slip planes are activated concurrently with the major crack propagation/ growth, as indicated by the slip bands visible in Figure 4(d, i). The individual slip bands are parallel to each other, each comprising multiple closely spaced parallel (0001) slip planes. The intersection of the slip bands with the particle surface generates straight slip steps (~70 nm width). This indicates that only the $\mathbf{b} = \frac{a}{3} < 11\bar{2}0 > (0001)$ type slip systems are activated

Batteries & Supercaps

Research Article
doi.org/10.1002/batt.202400077

Chemistry Europe
European Chemical
Societies Publishing

(Figure 4(g)), not alternative slip systems such as non-basal glide of $\mathbf{b} = \frac{a}{3} < 11\bar{2}0 >$ on prism $\{1\bar{1}00\}$ or pyramidal planes $\{1\bar{1}01\}$. There is also direct evidence that multiple $b = \frac{a}{3} < 11\bar{2}0 > (0001)$ slip systems can be activated in a single crystal particle. Specifically, the particle in Figure 4 (a-d) shears in two opposing directions on (0001), which can only be achieved by activation of at least two slip systems, either directly opposing each other, for example $\mathbf{b} = \frac{a}{3}[11\bar{2}0](0001)$ and $\mathbf{b} = \frac{a}{3}[\bar{1}\bar{1}20](0001)$, or by a combination of non-parallel Burgers vectors e.g. $\mathbf{b} = \frac{a}{3}[2\bar{1}\bar{1}0](0001)$ and $\mathbf{b} = \frac{a}{3}[\bar{1}2\bar{1}0](0001)$. A schematic showing the $\mathbf{b} = \frac{a}{3} < 11\bar{2}0 >$ type Burgers vectors lying in (0001) is shown in Figure 4(g). The activation of multiple slip systems can help accommodate the opposing stress either side of the indenter tip and enables the non-basal crack to widen (Figure 4(c)).

Prior to (0001) slip band formation, the NMC811 particles first fracture at the nanoscale, with sub-micron cracks nucleating (mode I) at the indenter tip/ particle contact zone. This occurred for compression tests on both (0001) and {012} facets (Figure 4(b, c) at 3.2 mN, and Figure 4(i, j) at 2.5 mN). The median cracks are oriented close to parallel to the loading axis, being non-basal for the (0001) facet, and close to basal for the {012} facet. Contact cracking is a known phenomenon in indentation of brittle materials, where the high, localised, tensile stress fields from sharp asperity contacts nucleate cracks to relieve stress.[24] For the sharp asperity contacts here, generated by using a 1 μm radius conospherical tip, the initial cracks in the NMC811 single crystals have < 50 nm width, and any associated dislocation activity is below the detection limit (no visible slip steps). At the higher stresses that activate crack propagation, opening, and particle failure, the

$b = \frac{a}{3} < 11\bar{2}0 > (0001)$ slip bands (Figure 4(d) and (k)) modify the shape of the non-basal cracks to accommodate the diamond asperity, resulting in a very rough, non-coplanar internal crack surface (Figure 4(d)). In comparison, the propagation of an internal crack on (0001) as a result of {012} facet compression, is planar (e.g. Figure 4(k)).

2.2. Effect of Single Crystal NMC811 Particle Size on Fracture Behavior

To evaluate the effect of particle size on fracture and slip band formation behavior, a smaller NMC811 particle (2.5 μm) was compressed to fracture on a {012} facet, to compare to the 3.9 μm particle in Figure 4(h–k). Figure 5(a–c) shows the dynamical SEM images of the 2.5 μm particle in situ compression test, Figure 5(d) the corresponding load-displacement curve, and Figure 5(e) a comparison of the load-displacement curves measured for the two NMC811 particles 2.5 μm, and 3.9 μm. An animated GIF of the in situ particle compression in Figure 5(a–c) is available in the supporting information (GIF 3). Initially the load-displacement curves have similar gradients (stiffness), however the smaller particle starts to plastically deform at a much lower load (~1.0 mN), and at 2.1 mN undergoes transparticle basal fracture (Figure 5(b)) at a mean contact pressure $p_m = 6$ GPa (compared to $p_m = 11$ GPa for the larger particle). In this small particle, a major crack propagates on (0001) fast through the whole particle. The crack propagation speed was significantly greater than raster speed of the SEM, resulting in particle movement mid-image (Figure 5(b)). Post-fracture, no slip bands were visible on the particle surface (Figure 5(c)). This
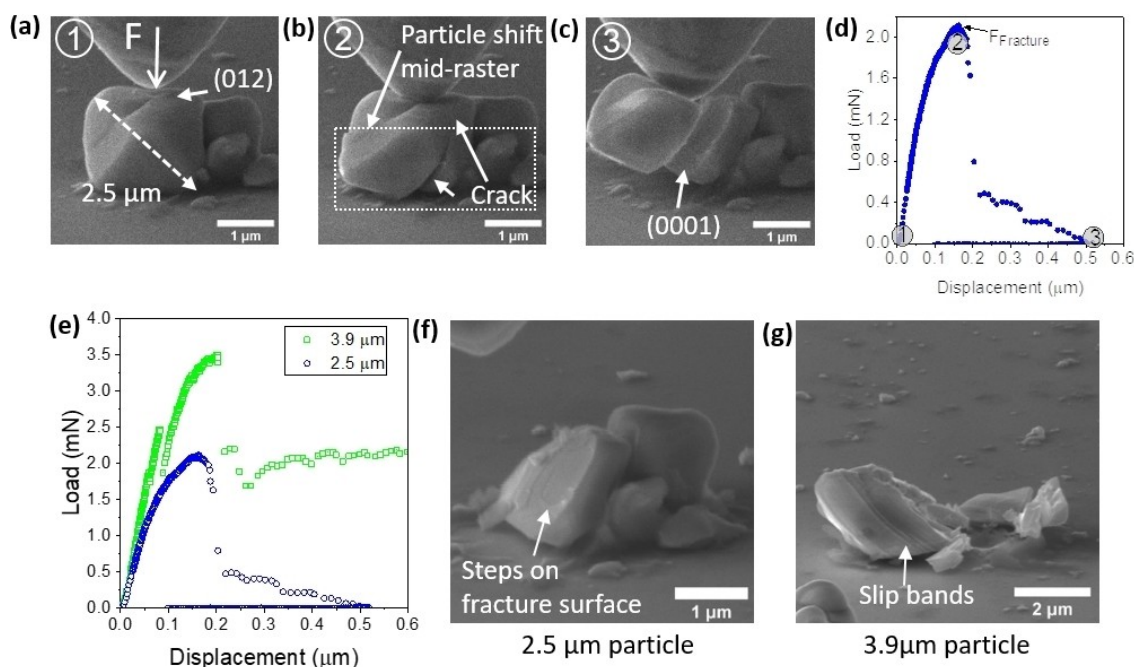

Figure 5. Dynamical SEM images of fracture of a 2.5 μm sized NMC811 particle compressed on {012}, with SEM images taken from the points labelled 1, 2, and 3 in the load-displacement curve in (d). (a) Point 1, pre-indentation, (b) Point 2, transparticle fracture, (c) Point 3, post compression. (e) Load-displacement curves for NMC811 particles fractured by applying a load to the {012} facet on particles of different diagonal lengths (3.9 μm, and 2.5 μm). (f) and (g) post compression SEM images of the fragmented 2.5 μm and 3.9 μm NMC811 particles respectively.

Batteries & Supercaps

Research Article
doi.org/10.1002/batt.202400077

Chemistry Europe
European Chemical
Societies Publishing

is different from the two-stage fracture mechanism of the larger particles (Figure 4 and Figure 5(g)), where the compressive stress field is more localised in the top half of the particle, and higher loads are required to first nucleate a crack, and then reach critical load for crack propagation and slip band growth.

The fractured NMC811 particle in Figure 5(a–c) is constrained on one side (to the right) by another particle, and in this case the basal crack widens from the base. This enables the left-hand particle fragment to rotate, facilitating further stress reduction by enabling the diamond asperity to displace downwards (Figure 5(b, d)). In a real electrode, the ability of a NMC particle to deform and rotate under asperity loading will depend on its local environment, including contact with surrounding NMC particles, carbon additives, and current collector.

Comparing the NMC811 particles compressed on {012} after compression (Figure 5(f, g) $\mathbf{b} = \frac{a}{3} < 11\bar{2}0 > (0001)$ slip bands are observed through the entire particle for the larger 3.9 μm particle. This particle continued to deform and rotate under continued compression at ~2 mN after the first major (0001) transparticle fracture (Figure 4(h–k)). This contrasts with the smaller 2.5 μm particle where a single (0001) transparticle fracture occurred, followed by particle fragment rotation and a load drop to < 0.5 mN (Figure 5(a–c)). Separation of the two particle fragments after the diamond tip is withdrawn enables examination of the basal fracture surface. It can be seen that at the nanoscale the (0001) fracture plane is not perfectly planar, exhibiting several concentric crack steps (Figure 5(f)). The preferred crack path can deviate due to the complex, time-dependant stresses within the fracturing particle as it changes shape. Also, although no discernible slip bands are visible in this case, localised stress changes due to the existence and propagation of intrinsic (growth) and deformation induced dislocations may also affect the crack path.

2.3. Consequences for Particle Fracture during Manufacture and Cycling of Single Crystal NMC811

The in situ mechanical testing of individual pristine NMC811 particles has highlighted key differences in the deformation and fracture mechanisms of single crystal NMC811 particles compared to polycrystalline NMC811. In situ, polycrystalline secondary particles NMC fail by progressive intergranular grain boundary crack propagation,[11] however for NMC811 single crystals the mechanical deformation sequence is observed to be initial submicron contact cracking (< 50 nm opening), followed by accelerated intragranular crack propagation/opening and concurrent (0001) slip band formation, dependant on the orientation of the $R\bar{3}m$ structure basal plane with respect to the principle load direction. The peak loads P_f sustained by the 2–4 μm diameter single crystals were 2–4.5 mN, similar to 6–8 μm diameter polycrystalline NMC811 secondary particles tested under similar conditions.[11] The corresponding peak pressures p_m sustained by the 2–4 μm diameter single crystals were 6–14 GPa, highest for particle loading down [0001].

In all compression tests carried out, the observed plastic deformation of NMC811 particles by dislocation glide generating slip steps, was only compatible with $\mathbf{b} = \frac{a}{3} < 11\bar{2}0 > (0001)$ slip systems (see Figure 4 and Figure 5). There was no evidence for non-basal glide of $\mathbf{b} = \frac{a}{3} < 11\bar{2}0 >$ on prism $\{1\bar{1}00\}$ or pyramidal planes $\{1\bar{1}01\}$), which may be due to strong O bonding,[5,20,21] or the energetically unfavourable glide of dislocations with non-basal Burgers vectors. As a consequence, the difficulty in mechanically activating 3-dimensional shear in pristine single crystal NMC811 particles will limit the material's ability to plastically deform.

In contrast, in polycrystalline particles, deformation and fracture is possible along multiple grain boundaries,[11] providing multiple 3D paths for stress release. The indentation strength for initiating mode I fracture from the surface of a polycrystalline NMC811 particle is 76 MPa,[11] less than the basal shear stress $\tau_c = 86$ MPa previously estimated for single crystals.[15] Indentation strength is not an intrinsic property, but dependent on the fracture toughness of the polycrystalline assembly, and the lower load required to initiate mode I fracture in polycrystalline NMC811 particles highlights the ease of stress release by crack propagation along grain boundaries. Polycrystalline NMC811 particles also experience additional tensile or compressive forces due to dimensional changes in neighbouring grains as in a polycrystalline architecture,[3] whereas single crystals will only experience local stresses arising at asperity contacts with neighbouring particles within electrodes and from chemical inhomogeneities arising from cycling.

Non-basal fracture is identified here as a key deformation mode in single crystal NMC811 particles, and occurs as a stress compensation mechanism due to the lack of multiple easily activated dislocation slip systems (Figure 4). In particular, non-basal fracture, the greatest load to fracture, and the greatest contact pressure at fracture, occur for compression normal to the (0001) layered structure where activation of $\mathbf{b} = \frac{a}{3} < 11\bar{2}0 > (0001)$ slip systems and basal fracture is the most difficult. This strong 3D mechanical anisotropy in the type of deformation activated (basal slip, basal fracture, non-basal fracture), and the load/pressure to fracture, all of which are dependent on the NMC811 crystal orientation with respect to the applied load, means that the distribution of the crystallographic orientations of the single crystals within an electrode (crystallographic texture of the electrode) will affect its mechanical response.

Rotation of individual NMC811 particles during compression, associated with fracture and slip band growth, was also observed here in situ as an effective mechanism to help accommodate the applied load (Figure 4 and Figure 5). In a real electrode, particle rotation may be locally constrained due to contacts with adjacent particles, particularly in highly calendered electrodes, and because the particles are bonded within a carbon-binder matrix. Stress on single crystal NMC811 particles at sharp asperity contacts from neighbouring particles, e.g. arising during electrode manufacture including during calendering or mixing, can result in cracking as a method to relieve stress where the particle is otherwise unable to rotate or accommodate the stress by basal shear. It should be noted that local stresses sufficient to cause single crystal NMC811

Batteries & Supercaps

Research Article
doi.org/10.1002/batt.202400077

Chemistry
Europe
European Chemical
Societies Publishing

particle fracture, measured here to be 6–14 GPa, can occur even at lower average pressures used in calendering or cold-pressing processes, due to stress concentration at the small contact areas of particle-particle contacts. Fracture of single crystal NMC811 has been previously reported resulting from calendering[15] and cycling.[19]

The NMC811 particles studied in this article are all in the pristine state. The case of cycled NMC811 will be different to pristine NMC811 as removal of Li, together with diffusion of transition metals and oxygen, changes the dislocation types that can form, and will introduce lattice defects arising from inhomogeneous diffusion. However, given the activation of basal-plane slip bands in the pristine material observed here, it is not surprising that planar gliding has been observed during cycling of $LiNi_{0.76}Mn_{0.14}Co_{0.1}O_2$ (NMC76) single crystals.[5,15,19,20] Slip band formation increases the surface area of a single NMC811 particle (Figure 5(g)), principally by small new (0001) facets. In comparison, the activation of basal and non-basal transparticle cracking can generate a significantly larger increase in particle surface area (Figure 4(d)). Any fracture in NMC cathode particles will be detrimental to cyclability, due to exposure of fresh surface to subsequent surface degradation from electrolyte, and potential for electrical isolation of fractured regions.

3. Conclusions

In this study we have evaluated the mechanical strength and real-time deformation mechanisms of individual single crystal particles of the key cathode material $LiNi_{0.8}Mn_{0.1}Co_{0.1}O_2$ (NMC811), under consideration to replace polycrystalline NMC811 materials. Employing a novel in situ SEM compression methodology enables the dynamical sequence of plastic deformation mechanisms within a single particle to be determined for the first time. In situ imaging identifies initial Mode I (opening) cracking at the compression zone, followed by accelerated transparticle crack propagation and associated (0001) slip band formation. It is clearly demonstrated that the mechanical deformation mechanisms activated within a NMC811 particle are a function of particle crystallographic orientation with respect to the principal load direction. Importantly, NMC811 particles compressed perpendicular to the (0001) layered structure are more mechanically resilient, exhibiting a higher load to activate initial crack propagation, and the greatest peak load P_f and mean contact pressure $p_m \sim 14$ GPa at fracture compared to particles compressed perpendicular to principal NMC811 single crystal {012} facets. This strong mechanical anisotropy is determined to originate from dislocation activity being restricted to 2D $\mathbf{b} = \frac{a}{3}<11\bar{2}0>(0001)$ slip systems on the basal plane, meaning that 3D stress fields cannot be fully accommodated by dislocation-driven plasticity. The dynamical imaging of single crystal particle mechanics in this work reveals a clear transition in cracking mechanisms from easy basal slip and (0001) basal cracking when loading on {012} crystal facets, to the activation of primary non-basal cracking with secondary basal cracking/slip when loading perpendicular

to the (0001) layered structure. Furthermore, for all orientations, the additional mode of particle rotation is observed to contribute to overall particle shape change under stress. Overall, this study significantly extends our understanding of the mechanical properties of Li-ion battery single crystal layered cathode materials. It highlights that key cathode design criteria to avoid detrimental particle fragmentation, and associated electrochemical degradation, should include optimising particle texture due to crystallographic dependent mechanical behaviour, maintaining a degree of particle mobility to enable rotational flexibility, and minimizing sources of localised surface stress in cathodes, e.g. particle-to-particle asperity contacts during electrode manufacture/calendering.

Experimental Methods

Synthesis of Faceted Single Crystal NMC811

Faceted single crystal NMC811 was synthesised via a two-step process as described elsewhere.[22] First a surfactant-modified $Ni_{0.8}Mn_{0.1}Co_{0.1}(OH)_2$ precursor material and $LiOH \cdot H_2O$ (M:Li ratio of 1:1.05) were mixed in a mortar and pestle. The mixture was pre-heated in a muffle furnace at 450 °C for 12 h, followed by microwave heating in air at 850 °C for 3 h, and tubular heating in an O_2 atmosphere at 850 °C for 3 h. Electrochemical cycling behavior of the single crystal NMC811 particles used in this study has been previously reported[22] and demonstrates a discharge capacity of 193 mAh g^{-1} when cycling at C/20 over the voltage ranges of 3.0–4.3 V vs. Li/ Li$^+$ at 25 °C.

Material Characterization

Powder X-ray diffraction (XRD) patterns were collected using a Rigaku Miniflex diffractometer at 40 kV, and 15 mA using Cu Kα radiation. Data was recorded from 10–>80° 2θ, with a step size of 0.02°. The XRD confirmed the NMC811 $R\bar{3}m$ structure, and unit cell sizes were refined using FullProf suite, giving a = 2.87 Å and c = 14.21 Å.

The faceted NMC811 particle morphology was imaged using scanning electron microscopy (SEM, FEI Inspect F) at 5 kV. Transmission Electron Microscopy (TEM) imaging and Selected Area Electron Diffraction (SAED) were performed to identify the facet planes of intact single crystal NMC811 particles using a JEOL JEM F200 TEM at 200 kV on NMC811 particles dispersed onto copper lace carbon grids (EM Resolutions). TEM images and SAED patterns were recorded using a Gatan One View camera. Patterns were indexed using Crystal Maker-Single Crystal software using the unit cell values calculated from the XRD analysis.

In situ SEM Microindentation of NMC811 Single Crystals

In situ SEM microindentation was performed on pristine faceted single crystal NMC811 particles mounted onto a Si wafer, adhered to an SEM stub. NMC811 particles were first sonicated for 40 mins in ethanol to ensure separation of the particles, and subsequently drop cast onto the Si wafer.

Fracture testing of the faceted single crystal NMC811 particles was performed with an Alemnis microindenter mounted in an FEI Nova 450 scanning electron microscope (SEM). Secondary electron (SE) imaging was performed in situ during the mechanical testing

at 70° to the indenter axis. Microindentation was performed with a 1 μm radius diamond cono-spherical indenter tip (Synton MDP) having Poisson's ratio – 0.07 and Young's modulus – 1140 GPa. Individual faceted single crystals could be selected for compression by moving the Alemnis translation stage such that the chosen particle was under the indentation tip. The particles were mechanically compressed under a ramped load control at 0.1 mN s^{-1}, concurrently measuring tip displacement and performing dynamical SEM imaging of the deformation and fracture sequence. When the particle fractured, the diamond tip was retracted to enable post-fracture imaging.

Microindentation load-displacement data was processed using Alemnis AMMDA software. The displacement was corrected to zero at zero load, and load drift corrections applied (using in-built polynomial fitting).

4. Supporting Information

Supporting Information is available from the Wiley Online Library.

Acknowledgements

Conflict of Interests

The authors declare no conflict of interest.

Data Availability Statement

The data that support the findings of this study are available in the supplementary material of this article.

[1] S. G. Booth, A. J. Nedoma, N. N. Anthonisamy, P. J. Baker, R. Boston, H. Bronstein, S. J. Clarke, E. J. Cussen, V. Daramalla, M. De Volder, S. E. Dutton, V. Falkowski, N. A. Fleck, S. H. Geddes, N. Gollapally, A. L. Goodwin, J. M. Griffin, A. R. Haworth, M. A. Hayward, S. Hull, B. J. Inkson, B. J. Johnston, Z. Lu, J. L. MacManus-Driscoll, X. Martínez De Irujo La-balde, I. McClelland, K. McCombie, B. Murdock, D. Nayak, S. Park, G. E. Pérez, C. J. Pickard, L. F. J. Piper, H. Y. Playford, S. Price, D. O. Scanlon, J. C. Stallard, N. Tapia-Ruiz, A. R. West, L. Wheatcroft, M. Wilson, L. Zhang, X. Zhi, B. Zhu, S. A. Cussen, *APL Mater.* **2021**, *9*, 109201.
[2] J. U. Choi, N. Voronina, Y.-K. Sun, S.-T. Myung, *Adv. Energy Mater.* **2020**, *10*, 2002027.
[3] W. M. Dose, J. K. Morzy, A. Mahadevegowda, C. Ducati, C. P. Grey, M. F. L. De Volder, *J. Mater. Chem. A* **2021**, *9*, 23582.
[4] W. M. Dose, W. Li, I. Temprano, C. A. O'Keefe, B. L. Mehdi, M. F. L. De Volder, C. P. Grey, *ACS Energy Lett.* **2022**, *7*, 3524.
[5] X. H. Meng, T. Lin, H. Mao, J. L. Shi, H. Sheng, Y. G. Zou, M. Fan, K. Jiang, R. J. Xiao, D. Xiao, L. Gu, L. J. Wan, Y. G. Guo, *J. Am. Chem. Soc.* **2022**, *144*, 11338.
[6] K. Ishidzu, Y. Oka, T. Nakamura, *Solid State Ionics* **2016**, *288*, 176.
[7] S. Li, Z. Jiang, J. Han, Z. Xu, C. Wang, H. Huang, C. Yu, S. J. Lee, P. Pianetta, H. Ohldag, J. Qiu, J. S. Lee, F. Lin, K. Zhao, Y. Liu, *Nat. Commun.* **2020**, *11*, 4433.
[8] Y. Mao, X. Wang, S. Xia, K. Zhang, C. Wei, S. Bak, Z. Shadike, X. Liu, Y. Yang, R. Xu, P. Pianetta, S. Ermon, E. Stavitski, K. Zhao, Z. Xu, F. Lin, X. Yang, E. Hu, Y. Liu, *Adv. Funct. Mater.* **2019**, *29*, 1900247.
[9] L. De Biasi, A. O. Kondrakov, H. Geßwein, T. Brezesinski, P. Hartmann, J. Janek, *J. Phys. Chem. C* **2017**, *121*, 26163.
[10] T. M. M. Heenan, A. Wade, C. Tan, J. E. Parker, D. Matras, A. S. Leach, J. B. Robinson, A. Llewellyn, A. Dimitrijevic, R. Jervis, P. D. Quinn, D. J. L. Brett, P. R. Shearing, *Adv. Energy Mater.* **2020**, *10*, 2002655.
[11] L. Wheatcroft, A. Bird, J. C. Stallard, R. L. Mitchell, S. G. Booth, A. J. Nedoma, M. F. L. De Volder, S. A. Cussen, N. A. Fleck, B. J. Inkson, *Batteries & Supercaps* **2023**, *6*, e202300032.
[12] J. C. Stallard, L. Wheatcroft, S. G. Booth, R. Boston, S. A. Corr, M. F. L. De Volder, B. J. Inkson, N. A. Fleck, *Joule* **2022**, *6*, 984.
[13] H. Liu, M. Wolf, K. Karki, Y. S. Yu, E. A. Stach, J. Cabana, K. W. Chapman, P. J. Chupas, *Nano Lett.* **2017**, *17*, 3452.
[14] L. S. De Vasconcelos, R. Xu, Z. Xu, J. Zhang, N. Sharma, S. R. Shah, J. Han, X. He, X. Wu, H. Sun, M. Perrin, X. Wang, Y. Liu, F. Lin, Y. Cui, K. Zhao, *Chem. Rev.* **2022**, *122*, 13043.
[15] J. C. Stallard, S. Vema, D. S. Hall, A. R. Dennis, M. E. Penrod, C. P. Grey, V. S. Deshpande, N. A. Fleck, *J. Electrochem. Soc.* **2022**, *169*, 040511.
[16] N. Sharma, D. Meng, X. Wu, L. S. de Vasconcelos, L. Li, K. Zhao, *Extreme Mech. Lett.* **2022**, *58*, 101920.
[17] D. Dang, Y. Wang, Y.-T. Cheng, *J. Electrochem. Soc.* **2019**, *166*, A2749.
[18] G. Qian, Y. Zhang, L. Li, R. Zhang, J. Xu, Z. Cheng, S. Xie, H. Wang, Q. Rao, Y. He, Y. Shen, L. Chen, M. Tang, Z. F. Ma, *Energy Storage Mater.* **2020**, *27*, 140.
[19] Y. Bi, J. Tao, Y. Wu, L. Li, Y. Xu, E. Hu, B. Wu, J. Hu, C. Wang, J. G. Zhang, Y. Qi, J. Xiao, *Science* **2020**, *370*, 1313.
[20] M. Sadowski, L. Koch, K. Albe, S. Sicolo, *Chem. Mater.* **2022**, *35*, 584.
[21] H. Gabrisch, R. Yazami, B. Fultz, *Electrochem. Solid-State Lett.* **2002**, *5*, A111.
[22] N. Gollapally, N. N. Anthonisamy, S. G. Booth, L. Wheatcroft, L. Middlemiss, I. Temprano, W. M. Dose, W. Li, B. L. Mehdi, S. W. T. Price, A. Vamvakeros, S. D. M. Jacques, Y. Odarchenko, j. Wright, E. J. Cussen, B. J. Inkson, S. A. Cussen, (Preprint) submitted: 2024.
[23] J. Zhu, G. Chen, *J. Mater. Chem. A* **2019**, *7*, 5463.
[24] D. B. Marshall, A. G. Evans, B. T. Khuri Yakun, J. W. Tien, G. S. Kino, *Proc. R. Soc. A* **1983**, *385*, 461.